Heteroatom-doped hierarchically porous thick bulk carbon derived from pleurotus eryngii/lignin composite: a free-standing and high mass loading electrode for high-energy-density storage

Weisheng Yang[a], Danning Wang[a], Shu Feng [a], Shuijian He [a], Huining Xiao[b], Hongqi Dai[c], Jingquan Han[a]*

[a] Jiangsu Co-innovation Center for Efficient Processing and Utilization of Forestry Resources, College of Materials Science and Engineering, Nanjing Forestry University, Nanjing, Jiangsu, 210037, China.

[b] Chemical Engineering Department, New Brunswick University, Fredericton, New Brunswick, E3B 5A3, Canada.

[c] College of Light Industry and Food Engineering, Nanjing Forestry University, Nanjing, Jiangsu, 210037, China.

* **Corresponding authors:**

Jingquan Han (Email: hjq@njfu.edu.cn)

S1 Characterization

The electrical conductivity of bulk carbon samples was measured using Four-Point Probes (4Probes Tech Ltd., RTS-9). The microstructure of bulk carbon samples was observed by field-emission scanning electron microscopy (FESEM, Zeiss Sigma 300) and transmission electron microscopy (TEM, JEM-2010EX). The surface wettability of bulk carbon samples was analyzed by a contact angle analyzer (OCA 15EC, Dataphysics, Germany). The volume of droplets for determination was set to 4 μL.

Raman spectra of bulk carbon samples were collected from a Raman spectrometer (Renishaw, inVia) ranging from 500-3000 cm^{-1} at an excitation wavelength of 532 nm. Bulk carbon samples were ground into powder for X-ray diffraction (XRD), Fourier Transform Infrared Spectroscopy (FT-IR), Brunauer Emmett Teller (BET) and X-ray photoelectron spectroscopy (XPS) analyses. XRD spectra were acquired using a Bruker D8 advance diffractometer operating with Cu Ka radiation, in the range of 5-80° at a scanning rate of 10°/min. The FTIR spectra (800–3800 cm^{-1}) were recorded on a Thermo scientific NicoletiS20 FTIR spectrometer with pure KBr as the background. The specific surface area and pore size distribution of samples were determined by N_2 adsorption-desorption using an ASAP2460 aperture analyzer. Prior to measurement, the samples underwent degassing at 180°C for 8 hours. The surface area was then calculated using the Brunauer-Emmett-Teller (BET) equation, and a plot of the pore size distribution was obtained from the adsorption branch of the isotherm using a non-local density functional theory (NLDFT) model. The chemical composition of carbon samples was analyzed by XPS (Thermo Scientific, K-Alpha) with a mono-chromicized Al Kα X-ray at 225 W.

S2 Electrochemical measurements

The electrochemical performance (Cyclic voltammetry (CV), Galvanostatic charge-discharge (GCD), electrochemical impedance spectroscopy (EIS)) of C-PE and C-PE-LS electrodes was evaluated by a three-electrode system using an electrochemical workstation (CHI 760e, CH Instruments, China). Briefly, the C-PE or C-PE-LS served as working electrodes, while the Pt foil and Ag/AgCl electrode served as the counter

and reference electrode in 1 M H_2SO_4 solution electrolyte. EIS was conducted at open circuit potential with an amplitude of 10 mV in a frequency range from 0.01 Hz to 100 kHz. The SSC device was assembled with two C-PE-LS electrodes using glass fiber filter as separator. The specific capacitance (Cm, F/g), areal capacitance (Cs, F/cm^2) and volume-specific capacitance (Cv, F/cm^3) of single electrodes and devices were calculated according to discharge curves using the following equations:

$$Cm = \frac{I \times dt}{m \times dv} \quad (1)$$

$$Cs = \frac{I \times dt}{s \times dv} \quad (2)$$

$$Cv = \frac{Cs}{d} \quad (3)$$

where I (A) was the current, dv was the operation voltage (V_{max}–IR_{drop}), m (g) was the mass of the individual electrode, S (cm^2) was the geometric area of the electrode, d (cm) was the thickness of electrode and dt (s) was the discharging time. For the devices, A was the geometric area of the electrode (cm^2).

The areal energy density (E, mWh/cm2) and power density (P, mW/cm^2) of the symmetric device were calculated using the following equations:

$$E_S = \frac{Cs \times dv^2}{2 \times 3.6} \quad (4)$$

$$P_S = \frac{3600 \times E_S}{t} \quad (5)$$

where Cs was the areal capacitance (F/cm^2), dv was the working voltage (V) and t was the discharging time (s) measured in the galvanostatic curves.

S3 DFT calculation methods

First-principles [1,2] were employed to perform spin-polarization density functional theory (DFT) calculations within the generalized gradient approximation (GGA) using the Perdew-Burke-Ernzerhof (PBE) [3] formulation. Projected augmented wave (PAW) potentials [4,5] were chosen to describe the ionic cores, and valence electrons were taken into account using a plane wave basis set with a kinetic energy cutoff of 450 eV. The Gaussian smearing method with a width of 0.05 eV was used to allow for partial occupancies of the Kohn-Sham orbitals. Self-consistency of the electronic energy was achieved when the energy change was less than 10^{-5} eV. Convergence of the geometry optimization was achieved when the energy change was less than 0.02 eV $Å^{-1}$. To eliminate artificial interactions between periodic images, a 18 Å vacuum layer was added to the surface. The DFT+D3 method with empirical correction in Grimme's scheme [6, 7] was used to describe the weak interaction.

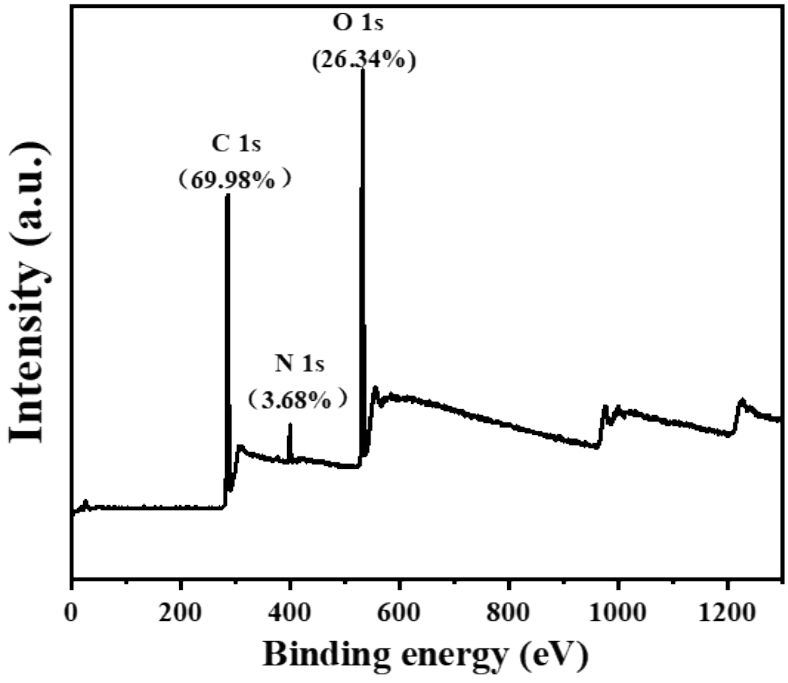

Figure S1 XPS analysis of PE aerogel.

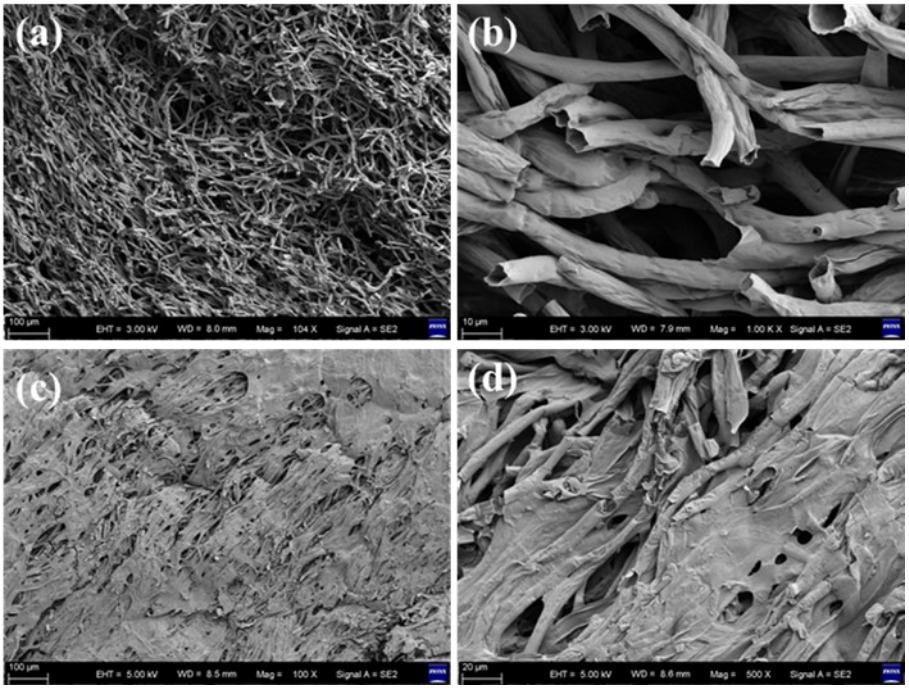

Figure S2 (a), (b) SEM images of section plane perpendicular to the growth direction of PE. **(c), (d)** SEM images of section in PE growth direction.

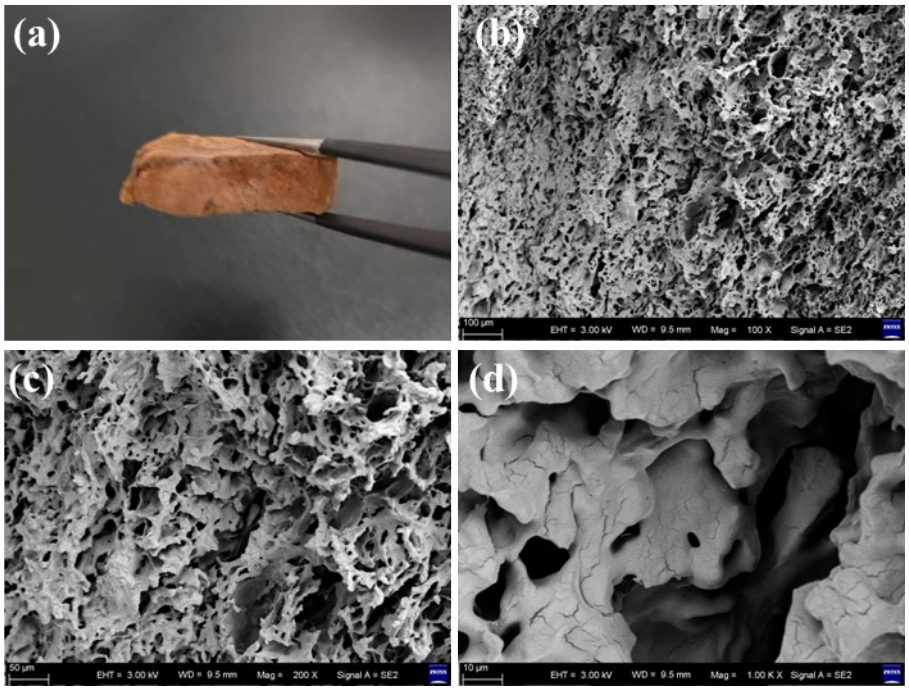

Figure S3 (a) The digital photograph of PE-LS composite. **(b-d)** SEM images of the interior of PE-LS aerogel.

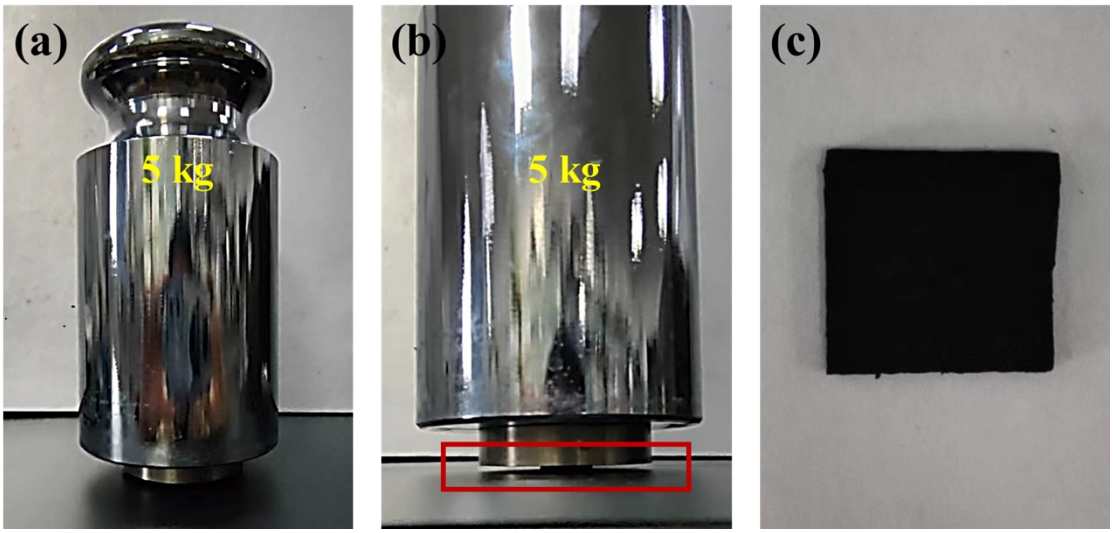

Figure S4 (a-b) C-PE-LS-KOH holds 5 kg of weight. **(c)** The morphology of C-PE-LS-KOH after being subjected to a 5 kg of weight.

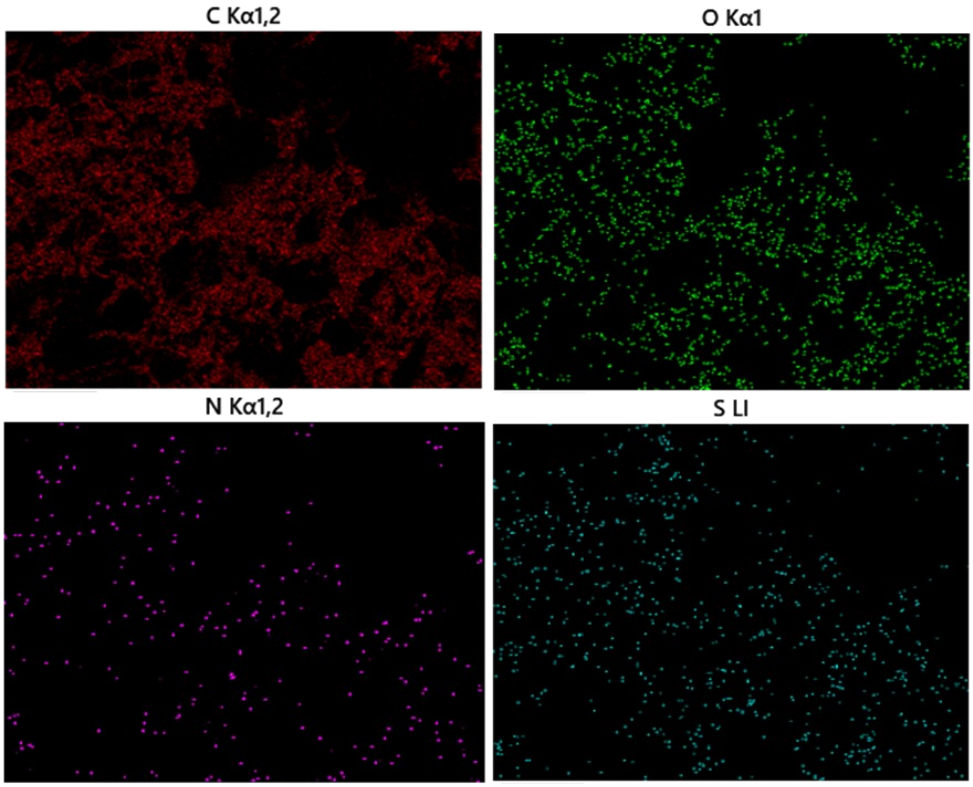

Figure S5 EDS analysis of C-PE-LS-KOH.

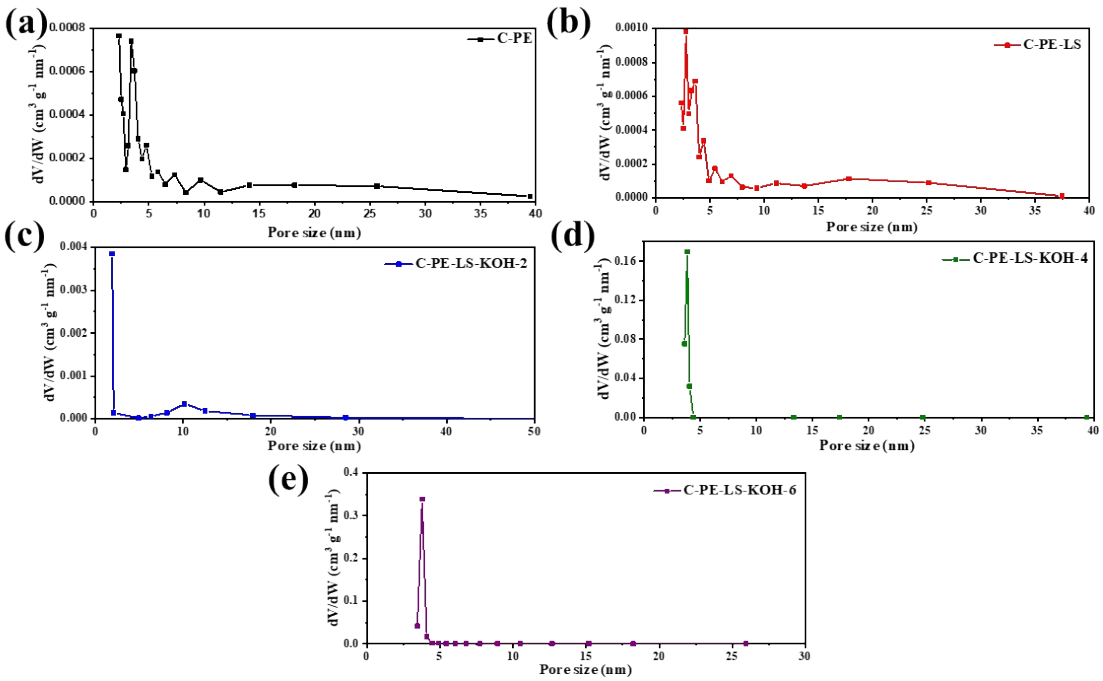

Figure S6 The pore distribution of C-PE, C-PE-LS, C-PE-LS-KOH-2, C-PE-LS-KOH-4, and C-PE-LS-KOH-6.

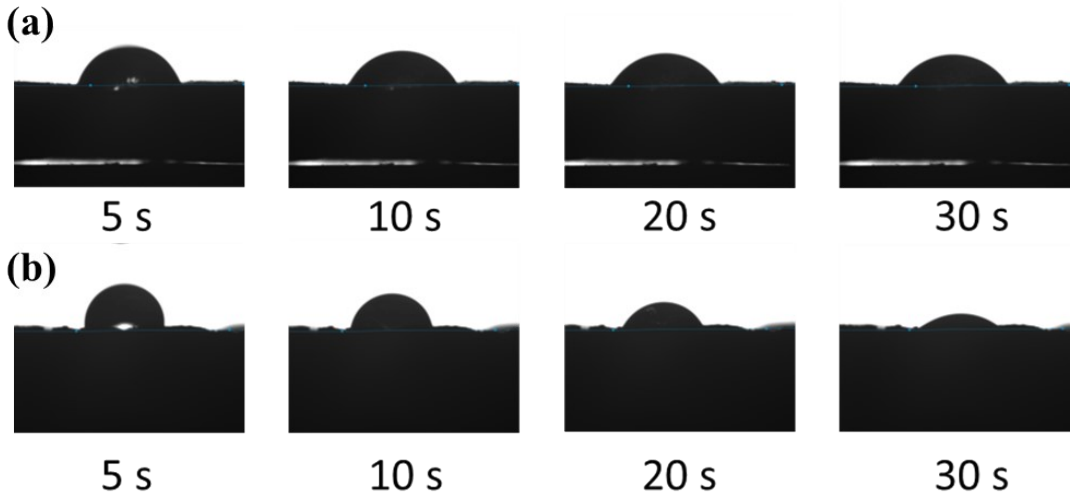

Figure S7 Contact angle of C-PE (a) and C-PE-LS-KOH-4 (b).

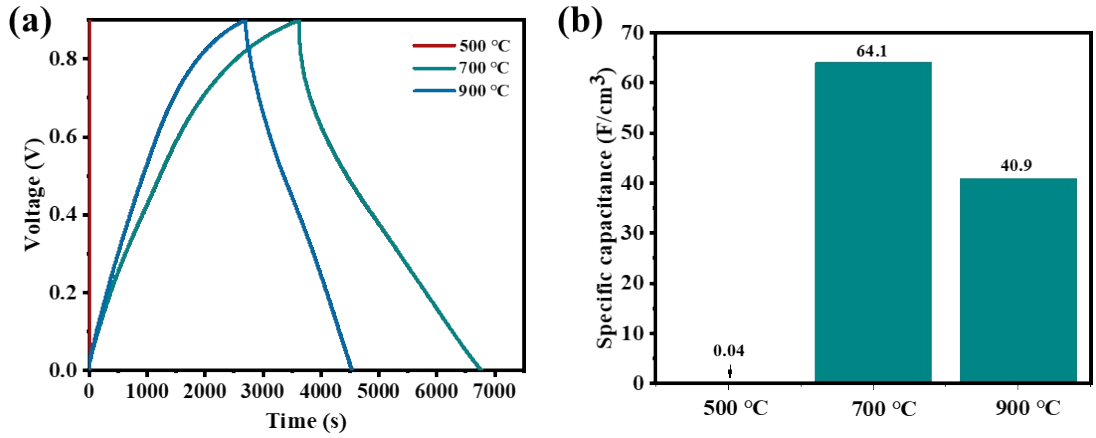

Figure S8 (a) The GCD curves of C-PE-LS-KOH-2 obtained under different temperatures of 500, 700, and 900 ℃, and the corresponding areal capacitances **(b)**.

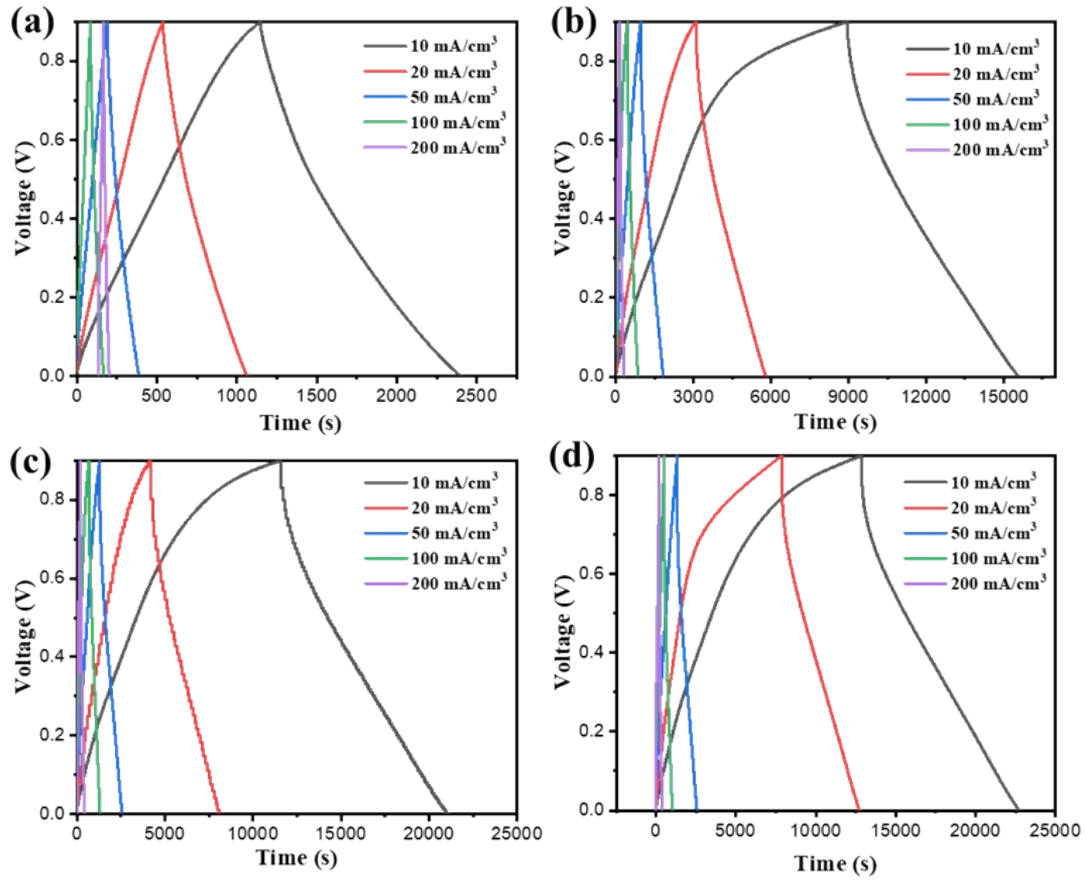

Figure S9 The GCD curves at various current densities of C-PE-LS, C-PE-LS-KOH-2, C-PE-LS-KOH-4, C-PE-LS-KOH-6.

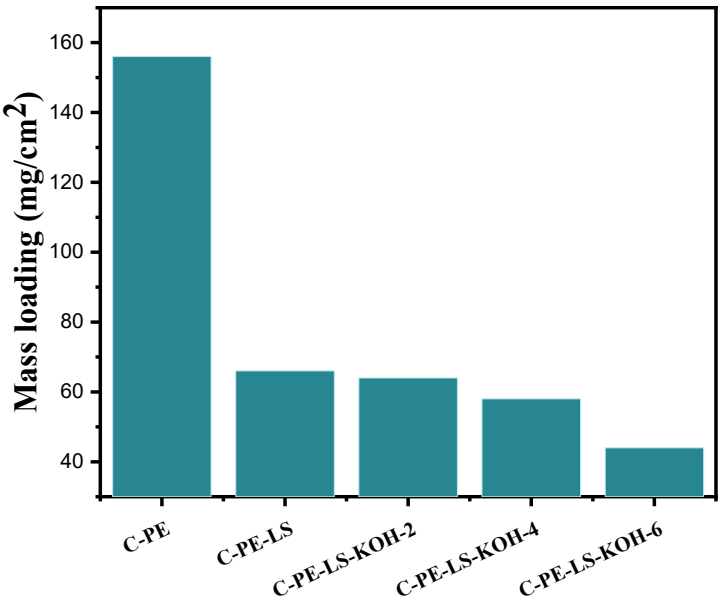

Figure S10 The mass loading of C-PE, C-PE-LS, C-PE-LS-KOH-2, C-PE-LS-KOH-4, and C-PE-LS-KOH-6.

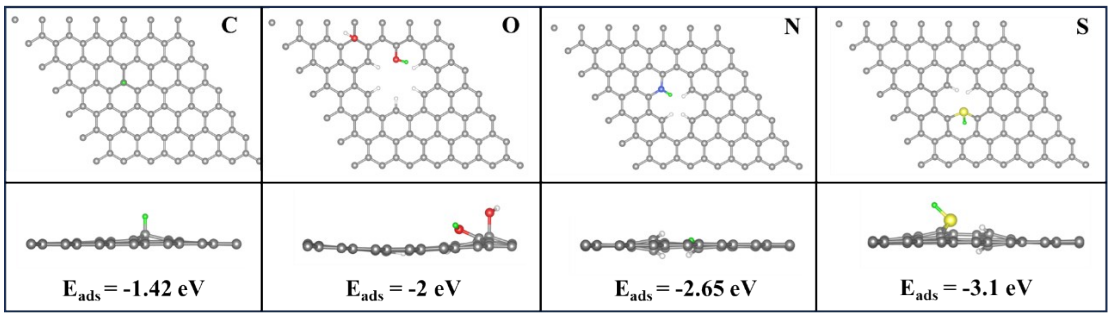

Figure S11 Graphite-H, Graphite-O-H, Graphite -N-H, and Graphite-S-H optimized geometry adsorbed structures.

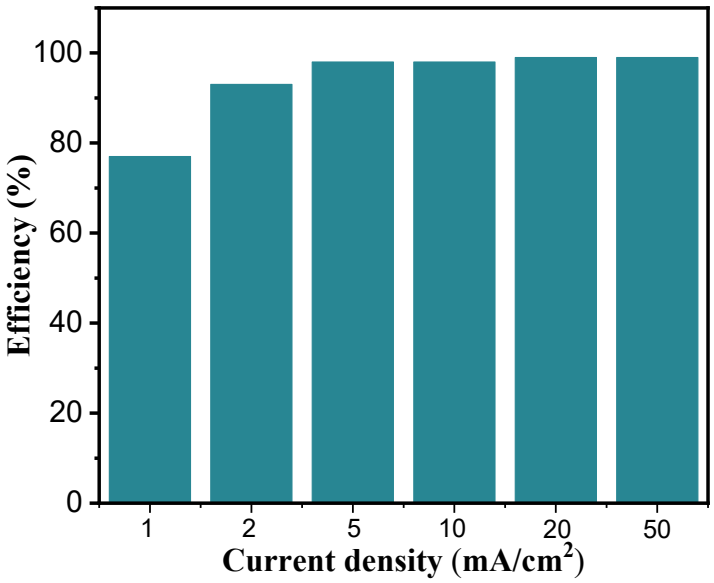

Figure S12 The charging and discharging efficiency of this SSC device at various current densities.

Table S1. Resistance determined according to Nyquist plots for the as-synthesized samples

Samples	C-PE	C-PE-LS	C-PE-LS-KOH-2	C-PE-LS-KOH-4	C-PE-LS-KOH-6
Rs(Ω)	1.60	1.33	1.76	1.79	1.90
Rct(Ω)	6.98	0.89	1.00	1.76	2.39

Table S2. Comparison of areal capacitance, energy density, and thickness of our SSC devices with other reported other state-of-the-art supercapacitors.

Ref.	Areal capacitance (F/cm^3)	Energy density (mWh/cm^3)	Thickness (mm)
This work	12.80	2.56	4
8	3.94	0.55	3
9	0.85	0.94	4
10	18.74	1.56	8
11	6.21	1.86	2
12	1.36	0.3	6
13	4.70	0.94	1.6
14	1.5	0.21	1.6
15	3.62	0.50	1.6
16	3.29	0.89	4
17	0.64	0.05	2

[1] Kresse, G.; Furthmüller, J. Efficiency of Ab-Initio Total Energy Calculations for Metals and Semiconductors Using a Plane-Wave Basis Set. Comput. Mater. Sci. 1996, 6, 15−50.
[2] Kresse, G.; Furthmüller, J. Efficient Iterative Schemes for Ab Initio Total-Energy Calculations Using a Plane-Wave Basis Set. Phys. Rev. B 1996, 54, 11169−11186.
[3] Perdew, J. P.; Burke, K.; Ernzerhof, M. Generalized Gradient Approximation Made Simple. Phys. Rev. Lett. 1996, 77, 3865−3868.
[4] Kresse, G.; Joubert, D. From Ultrasoft Pseudopotentials to the Projector Augmented-Wave Method. Phys. Rev. B 1999, 59, 1758-1775.
[5] Blöchl, P. E. Projector Augmented-Wave Method. Phys. Rev. B 1994, 50, 17953-17979.
[6] S. Grimme, J. Antony, S. Ehrlich, and S. Krieg, J. Chem. Phys. 2010，132, 154104.
[7] S. Grimme, S. Ehrlich, and L. Goerigk, J. Comp. Chem. 2011，32, 1456.

[8] Zhang, W.; Li, M.; Zhong, L.; Huang, J.; Liu, M., A family of MOFs@ Wood-Derived hierarchical porous composites as freestanding thick electrodes of solid supercapacitors with enhanced areal capacitances and energy densities. Materials Today Energy 2022, 24, 100951.
[9] Yao, B.; Chandrasekaran, S.; Zhang, H.; Ma, A.; Kang, J.; Zhang, L.; Lu, X.; Qian, F.; Zhu, C.; Duoss, E. B., 3D-printed structure boosts the kinetics and intrinsic capacitance of pseudocapacitive graphene aerogels. Advanced materials 2020, 32 (8), 1906652.
[10] Yao, B.; Chandrasekaran, S.; Zhang, J.; Xiao, W.; Qian, F.; Zhu, C.; Duoss, E. B.; Spadaccini, C. M.; Worsley, M. A.; Li, Y., Efficient 3D printed pseudocapacitive electrodes with ultrahigh MnO2 loading. Joule 2019, 3 (2), 459-470.
[11] Yan, B.; Feng, L.; Zheng, J.; Zhang, Q.; Jiang, S.; Zhang, C.; Ding, Y.; Han, J.; Chen, W.; He, S., High performance supercapacitors based on wood-derived thick carbon electrodes synthesized via green activation process. *Inorganic Chemistry Frontiers* **2022,** *9* (23), 6108-6123.
[12] Liu, K.; Mo, R.; Dong, W.; Zhao, W.; Huang, F., Nature-derived, structure and function integrated ultra-thick carbon electrode for high-performance supercapacitors. Journal of Materials Chemistry A 2020, 8 (38), 20072-20081.
[13] Wang, F.; Cheong, J. Y.; He, Q.; Duan, G.; He, S.; Zhang, L.; Zhao, Y.; Kim, I.-D.; Jiang, S., Phosphorus-doped thick carbon electrode for high-energy density and long-life supercapacitors. Chemical Engineering Journal 2021, 414, 128767.
[14] Wang, X.; Yang, C.; Li, J.; Chen, X. a.; Yang, K.; Yu, X.; Lin, D.; Zhang, Q.; Wang, S.; Wang, J., Insights of heteroatoms doping-enhanced bifunctionalities on carbon based energy storage and conversion. Advanced Functional Materials 2021, 31 (11), 2009109.
[15] Chen, L.; Wang, F.; Tian, Z.; Guo, H.; Cai, C.; Wu, Q.; Du, H.; Liu, K.; Hao, Z.; He, S., Wood-Derived High-Mass-Loading MnO2 Composite Carbon Electrode Enabling High Energy Density and High-Rate Supercapacitor. Small 2022, 18 (25), 2201307.
[16] Xue, J.; Gao, L.; Hu, X.; Cao, K.; Zhou, W.; Wang, W.; Lu, Y., Stereolithographic 3D printing-based hierarchically cellular lattices for high-performance quasi-solid supercapacitor. Nano-Micro Letters 2019, 11, 1-13.
[17] Tang, X.; Zhou, H.; Cai, Z.; Cheng, D.; He, P.; Xie, P.; Zhang, D.; Fan, T., Generalized 3D printing of graphene-based mixed-dimensional hybrid aerogels. ACS nano 2018, 12 (4), 3502-3511.